Green Chemical Technology

SCIEPublish

Article

Crystal Facet-Dependent Reactivity of Cu_2O in Direct Synthesis of Tetraethoxysilane from Silicon and Ethanol

Jingyu Feng [1], Yuhe Ran [1], Zhongjun Li [2], Guojing Wang [1], Shengchao Qiu [1,2], Renliang Lyu [1,3,*] and Ru'an Chi [1,3]

[1] Laboratory of Green Chemical Technology, Hubei Three Gorges Laboratory, Yichang 443000, China; fengjingyu@hbsxsys.com (J.F.); ranyuhe@hbsxsys.com (Y.R.); wangguojing@hbsxsys.com (G.W.); qiushengchao@hbsxsys.com (S.Q.); rac@wit.edu.cn (R.C.)

[2] Hubei Xingfa Chemicals Group Co., Ltd., Yichang 443000, China; lizhongjun@hbsxsys.com (Z.L.)

[3] State Key Laboratory of Green and Efficient Development of Phosphorus Resources, Key Laboratory for Green Chemical Engineering Process of Ministry of Education, School of Chemical Engineering and Pharmacy, Wuhan Institute of Technology, Wuhan 430205, China

* Corresponding author. E-mail: lyurenliang@wit.edu.cn (R.L.)

Received: 27 May 2026; Revised: 2 June 2026; Accepted: 15 September 2026; Available online: 28 September 2026

ABSTRACT: Ethanol can react with active metals to form alkoxides and hydrogen gas, but metallic silicon exhibits relatively stable chemical properties and does not react with ethanol significantly under catalyst-free and low-temperature conditions. Previous research on organosilicon synthesis has primarily focused on the Rochow reaction, in which metallic silicon reacts with methyl chloride. The extension of copper-based catalysts from the Rochow reaction to enable the direct reaction of metallic silicon with ethanol, in which silicon replaces the hydroxyl hydrogen of ethanol to form silanes, has attracted widespread interest. In this study, we synthesized Cu_2O with well-defined exposed crystal facets via facet engineering, modulating the surface facet ratios and systematically investigating the effects of these Cu_2O with different morphologies on the direct reaction. Combining advanced spectroscopic techniques, density functional theory calculations, and molecular dynamics simulations, we revealed that Cu_2O (111) exhibits the highest surface oxygen vacancy concentration and hydroxyl density. The oxygen vacancies on the Cu_2O (111) surface facilitated the adsorption of ethanol, while the surface hydroxyl groups effectively promoted ethanol dehydrogenation. These two effects work in concert to render the Cu_2O (111) facet the highest facet-dependent chemical reactivity in the direct reaction of metallic silicon and ethanol relative to those from other facets. Our study provides crucial insights into the cooperative roles of exposed active sites and surface crystal planes that are potentially relevant to heterogeneous catalysis. Furthermore, this work proposes an understanding of product selectivity to guide the development of other copper-based catalysts for the direct synthesis strategy.

Keywords: Metallic silicon; Rochow reaction; Cu_2O; Direct reaction; Oxygen vacancy

© 2026 The authors. This is an open access article under the Creative Commons Attribution 4.0 International License (https://creativecommons.org/licenses/by/4.0/).

1. Introduction

Tetraethoxysilane (TEOS) is a pivotal precursor in silane coupling chemistry and sol-gel processes, and it plays an indispensable role in the fabrication of silica-based functional materials, ceramic coatings, and electronic packaging media [1–3]. Conventional industrial production involves oxidizing metallic silicon (Si_{met}) to synthesize +4 oxidation-state silicon intermediates, such as dimethyldichlorosilane (Me_2SiCl_2, M2), $HSiCl_3$, or $SiCl_4$, followed by stepwise alcoholysis with ethanol (EtOH). Although this technology is already mature, it requires the use of highly corrosive raw materials and is accompanied by the generation of substantial gaseous by-products (HCl), leading to equipment corrosion, environmental pollution, and high post-treatment costs [4,5]. In recent years, the direct synthesis strategy based on the concept of green chemistry has attracted much attention, researchers have attempted to synthesize TEOS by directly reacting silica (SiO_2) with EtOH, but this route has high requirements for SiO_2 [6–10]. It is well known that silicon oxide is one of the most stable oxides and has an extremely high Si–O bond energy. Therefore, the Si–O bond is difficult to break, making it difficult to form new chemical bonds. Most research reports have focused on the utilization of biomass SiO_2 or other amorphous SiO_2 with higher reactivity, but the experimental results show that its reaction efficiency is still at a relatively low level and does not have industrial significance [11,12].

In our previous research, we employed ammonium fluoride (NH_4F) treatment to convert quartz sand into amorphous silica. Through closed-loop recycling of NH_4F to reduce production costs, we achieved TEOS synthesis directly from silica [13]. However, the yield remained unsatisfactory. Given the inherent challenges in activating SiO_2 due to its high Si–O bond energy (452 kJ/mol), the organosilicon industry inevitably relies on high-temperature carbothermal reduction to convert SiO_2 to Si_{met} [14]. Consequently, Si_{met} serves as a cost-effective and readily available raw material for industrial processes. Since the "direct synthesis" of methylchlorosilanes from Si_{met} and methylchloride (MeCl) was discovered by Rochow [15,16], the mechanism of the catalytic process has been under consideration. However, despite many efforts, obtaining effective catalysts remains a challenge. Various forms of metallic copper [17,18], its (I) and (II) salts [19,20] or oxides [21–23], as well as the different copper-containing composites and mixtures [24] are known to be catalytically active for the so-called "direct synthesis". However, in addition to the desired M2 in the Rochow reaction, these catalysts also lead to the generation of other methylchlorosilane monomer products. This consequently elevates the complexity of separation and purification processes.

In order to achieve higher atom economy, researchers have begun exploring whether catalysts of analogous chemical composition can catalyze the direct reaction between Si_{met} and EtOH as shown in Equation (1) [25]. This novel pathway eliminates the need for chlorosilane alcoholysis, simultaneously avoiding the introduction of Cl and the generation of substantial byproducts, with hydrogen as the sole by-product. Based on extensive experimental data and practical applications, we unexpectedly identified cuprous oxide (Cu_2O) as markedly more applicable than CuCl, contrary to prevailing literature consensus [26,27]. As a low-cost and structurally tunable p-type semiconductor, Cu_2O exhibits unique advantages in reactions involving C–O bond coupling and CO_2 reduction due to its facet-dependent catalytic properties [28–33]. Theoretical studies indicate that distinct exposed crystal facets of Cu_2O (e.g., {100}, {111}, or {110}) significantly modulate the local charge distribution at active sites and the substrate adsorption strength, owing to differences in surface atomic coordination and electronic structure [34,35]. For instance, the high density of Cu^+ sites on {110} facets may enhance polarization and activation of surface Si–OH groups in Si_{met} during direct reaction with EtOH. Conversely, oxygen vacancies enriched on {111} facets favor the adsorption and deprotonation of ethanol molecules. These effects synergistically promote the directional formation of Si–O–C bonds. However, the mechanistic understanding of Cu_2O facet effects in this specific reaction remains unexplored. Crucially, the effect of facet engineering on reaction pathway selectivity and kinetic efficiency in TEOS synthesis remains to be elucidated.

This study focuses on the crystal facet effects of Cu_2O as an additive in the direct synthesis. We controllably synthesized Cu_2O with selectively exposed facets and systematically investigated their reactivity performance in the reaction of Si_{met} with EtOH for TEOS synthesis (as shown in Figure 1). Through integrated structural characterization and density functional theory (DFT) calculations, we elucidated the dynamic roles of distinct facets in modulating adsorption configurations and EtOH deprotonation activation. This enabled us to establish facet-dependent principles for regulating the reactivity and selectivity of the reaction, ultimately identifying the optimal Cu_2O structure with the highest promoting efficiency. However, both trialkoxysilanes (TES) and TEOS were formed in this system, which gives rise to the challenge of achieving high selectivity toward the target product TEOS. We thus adopted a high-pressure reactor with a stoichiometric excess of EtOH to address this issue. On the one hand, EtOH serves as a solvent to enhance the interfacial contact between Si_{met} and Cu_2O. On the other hand, the excess EtOH thermodynamically shifts the reaction equilibrium toward TEOS formation (Equation (2)), thereby boosting the selectivity and yield of TEOS. Simultaneously, we mechanistically probed the conversion pathway from TES to TEOS. This work thus provides a basis for the rational design of efficient reaction systems for TEOS synthesis and offers insights that may inform the development of green manufacturing technologies in the organosilicon industry.

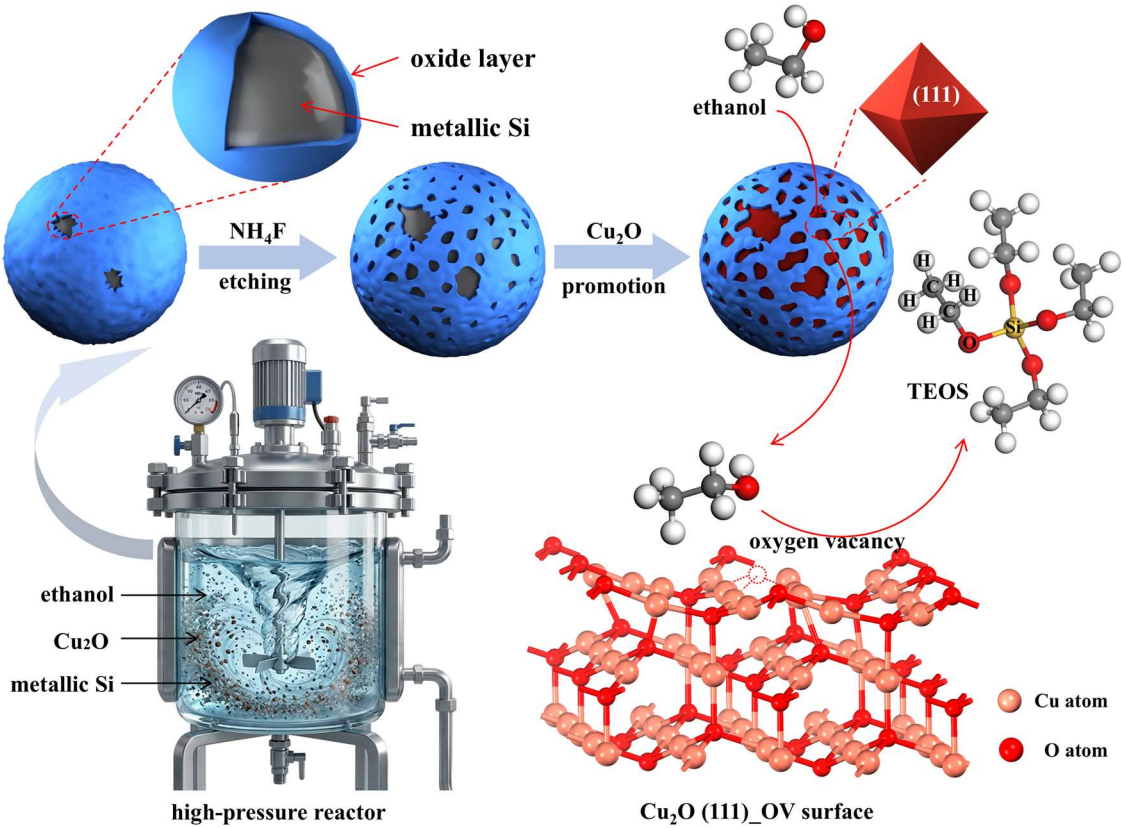

Figure 1. Schematic diagram of the synthesis strategy based on the crystal plane effect of Cu_2O for the direct reaction of metallic Si and ethanol.

$$Si + 3ROH \rightarrow HSi(OR)_3 + H_2 \quad (1)$$

$$HSi(OR)_3 + ROH \rightarrow Si(OR)_4 + H_2 \quad (2)$$

$$2ROH \rightarrow R_2O + H_2O \quad (3)$$

$$ROH + H_2 \rightarrow RH + H_2O \quad (4)$$

$$Cu_2O + H_2 \rightarrow 2Cu + H_2O \quad (5)$$

2. Experimental Section

2.1. Synthesis and Regulation of Cu_2O Nanocrystals

In a typical method [36], Cu_2O nanocrystals were synthesized by liquid-phase precipitation method, and the crystal planes of Cu_2O were regulated by PVP. Firstly, 0.5 L of a 10 mM $CuCl_2{\cdot}2H_2O$ solution (with 25 mmol, 50 mmol g, 75 mmol, 100 mmol and 125 mmol of PVP for Cu_2O with different morphologies) was poured into a beaker and kept in a water bath under 55 °C with magnetic stirring for 30 min to obtain a pale blue solution. Subsequently, 50 mL of NaOH solution (2 M) was added to the container, and the mixture was stirred for another 30 min. The solution changes from blue to green and eventually to dark brown. Then, 50 mL of AA solution (0.6 M) was used as the reductant to reduce Cu^{2+} to Cu^{+} for 30 min of stirring and was aged for 3 h. The brick red precipitation was washed and centrifuged with deionized water and ethanol for three times, finally dried in a vacuum at 60 °C for 5 h, and obtained the specified morphology of Cu_2O.

2.2. Direct Synthesis of TEOS from Si_{met} and EtOH with Cu_2O

A 20 wt% NH_4F solution was prepared for silicon surface pretreatment. Silicon powder was immersed in the NH_4F solution for 1 h to etch oxide layer, followed by washing and vacuum drying. Subsequently, 10 g of pre-treated silicon powder was thoroughly mixed with 0.5 g Cu_2O using an agate mortar. The mixed powder was loaded into alumina combustion boats and calcined (400 °C, 1 h) under N_2 atmosphere (flow rate: 50 mL/min) in a tube furnace (LC-SK4-20-12TP, Shanghai Lichen-BX Instrument Technology Co., Ltd., Shanghai, China) with a heating ramp of 5 °C/min. TEOS synthesis was conducted in a mechanically agitated high-pressure reactor (YZRJ-250, Shanghai Yanzheng Experimental Instrument Co., Ltd., Shanghai, China). Calcined silicon-copper composites were combined with 100 mL anhydrous ethanol in the reactor liner. The system was purged with N_2 (3×) to displace atmospheric gases before heating to 200 °C under continuous stirring (600 rpm) to prevent sedimentation. After maintaining reaction conditions for 1 h, the system was cooled to room temperature. The product was centrifuged (8000 rpm, 10 min) for liquid-solid separation prior to compositional analysis and material characterization.

2.3. GC-MS Analysis Conditions

The chromatographic column is HP-5MS (30.0 m × 250 μm, 0.25 μm), the initial temperature is maintained at 100 °C for 2 min, then increased at a rate of 10 °C/min to 170 °C and held for 5 min. The vaporization chamber temperature is 170 °C, and the transfer line temperature is 200 °C. The carrier gas is He, and the carrier gas flow rate is 1.0 mL/min. The split ratio is 30:1, and the injection volume is 1 μL.

Mass spectrometry conditions: EI source, electron energy 70 eV, scanning mode is Scan, scanning mass range is 35~500 u, solvent delay 3 min.

2.4. DFT Calculations

Spin-polarized density functional theory (DFT) calculations were performed using the CASTEP program package in Materials Studio (23.1.0.3829). Generalized gradient approximation (GGA) with Perdew-Burke-Ernzerhof (PBE) functional [37] was selected for exchange and correlation potentials. The energy cutoff for the plane wave expansion was set to 450 eV, and 0.03 eV/Å was used for the convergence criterion of geometry relaxation. The Gaussian smearing method with a smearing width of 0.05 eV was

used to determine partial occupancies. A 15 Å vacuum was added along the z direction to avoid the interaction between periodic structures. The Brillouin zone integration was performed using 3 × 3 × 1 k-point sampling. The self-consistent calculations applied a convergence energy threshold of 10^{-4} eV. The DFT-D3 method was employed to consider the van der Waals interaction. The on-site Coulomb interaction between 3d electrons of Cu was considered by GGA + U with a U-J value of 4 eV proposed by Li et al. [38] for Cu_2O system.

We constructed Cu_2O (100), Cu_2O (111), and Cu_2O (111)_OV slab models to understand the crystal plane-controlled effect of Cu_2O. For the Cu_2O (100) surface, a 2 × 2 surface unit cell with a size of 8.605 Å ×8.605 Å was considered. A super cell containing nine-atomic layers Cu_2O periodic slab was constructed from an optimized Cu_2O crystal, in which the top three layers were allowed to relax, and the bottom six layers were fixed. A 2 × 2 unit cell with a size of 12.169 Å × 12.169 Å was used for the Cu_2O (111) surface. The slab model also contained nine-atomic layers, the top three layers were allowed to relax, and the bottom six layers were fixed. Then, a surface oxygen vacancy was created on the perfect Cu_2O (111) surface to study the effect of surface defects on surface activity. The established slab models of nonpolar Cu_2O are shown in Figure S1.

3. Results and Discussion

3.1. Nanostructure Evolution of Cu_2O Cube to Octahedron

Cu_2O crystallizes in the cubic crystal system, exhibiting significant differences in surface energy among its various facets. The low-index {100}, {111}, and {110} planes are the most extensively studied, with distinct atomic arrangements on these facets leading to substantial variations in the morphology and properties of Cu_2O crystals [39]. The {100} and {111} facets represent the most thermodynamically stable and readily synthesized planes of Cu_2O. This inherent stability facilitates their preferential formation and enables precise morphological control via surface capping agents in precipitation synthesis. Liquid-phase precipitation offers additional advantages, including short reaction times, straightforward processing, and excellent potential for industrial scalability. Figure 2 shows the SEM images of Cu_2O crystals synthesized at varying polyvinylpyrrolidone (PVP) concentrations. In the absence of PVP, Cu_2O crystals adopted an equilibrium morphology characterized by minimal total surface energy. Among the major planes of Cu_2O, the {100} planes exhibit the lowest surface energy. Consequently, in the absence of any additives, the thermodynamically stable morphology of Cu_2O was a cube (Cu_2O-c) bounded by six equivalent {100} facets (Figure 2a). Upon introduction of PVP into the reaction solution, the carbonyl groups (C=O) and pyrrolidone rings of PVP chains formed weak coordination complexes with Cu^+ ions. This induced preferential adsorption of PVP onto the high-surface-energy {111} planes of Cu_2O crystal seeds. The adsorption lowered the surface energy of the {111} planes, promoting their exposure during crystal growth [40]. Consequently, the morphology evolved into truncated cubes (Cu_2O-tc), where the eight newly formed faces at the cube corners corresponded to the {111} facets, the corresponding morphologies of which are shown in Figure 2b. With further increases in PVP concentration, the relative area of {111} facets expanded. Adjacent {111} facets on neighboring truncations intersected to form new edges, transforming each {111} face from triangular to hexagonal and yielding vertex-truncated octahedrons (Figure 2c,d), which are bounded by six square {100} facets and eight hexagonal {111} facets. Continued growth promoted further expansion of {111} facets at the expense of {100} facets. When the expanding {111} facets fully surrounded each diminishing {100} facet, the shared of {100} and {111} facet boundaries coalesced, causing the hexagonal {111} faces to revert to triangular facets. Ultimately, this process yielded a high-symmetry octahedron (Cu_2O-o) exclusively enclosed by eight triangular {111} facets (Figure 2e).

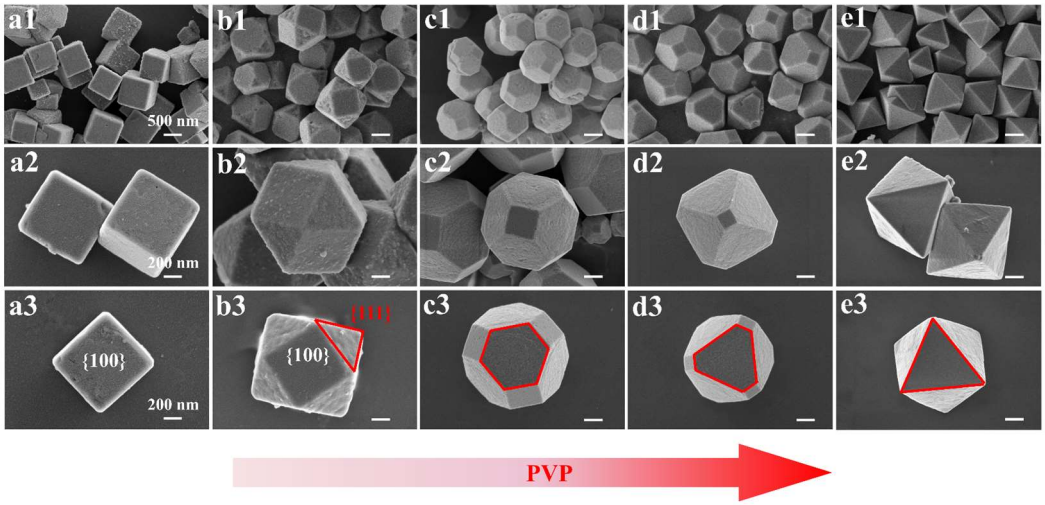

Figure 2. FESEM images of the Cu_2O polyhedrons with different volume ratios of {100} to {111}. (**a1**–**a3**) = 25 mmol PVP, (**b1**–**b3**) = 50 mmol PVP, (**c1**–**c3**) = 75 mmol PVP, (**d1**–**d3**) = 100 mmol PVP, (**e1**–**e3**) = 125 mmol PVP. The facets composed by the red lines represent the {111} facets. Scale bar = 500, 200, 200 nm, respectively.

The increasing surface ratio of {111} to {100} was further confirmed by X-ray powder diffraction (XRD) characterization. As shown in Figure S2, characteristic diffraction peaks were observed at 29.5°, 36.4°, 42.3°, 61.3°, and 73.5°, which were designated to Bragg reflections of (110), (111), (200), (220), and (311) crystal planes of Cu_2O (PDF#05-0667), respectively. No other copper species (e.g., Cu^0 or CuO) were detected, indicating successful synthesis of phase-pure Cu_2O. Quantitative analysis revealed a progressive increase in the intensity ratio of (111)/(200) peaks from 2.70 to 2.80, 2.84, 2.89, and 2.96 during the morphological transition towards octahedra. This statistically significant increase quantitatively corroborated the enhanced dominance of {111} planes exposure [41].

The quantified crystallographic features regarding the exposed surfaces of these architectures were proved by TEM observations and the corresponding selected area electron diffraction (SAED) analysis viewed along a series of important low miller index directions. As shown in Figure 3a, alignment of the electron beam perpendicular to the {100} facets of Cu_2O-c yielded an exclusive two-dimensional square projection. HRTEM imaging of this surface revealed highly ordered lattice fringes with a measured spacing of 0.216 nm (Figure 3d), corresponding to the (200) planes of Cu_2O (PDF#05-0667). Given that (200) reflections represent diffraction manifestations of the (100) family rather than distinct physical planes, these facets were unequivocally identified as {111}. Figure 3b displays Cu_2O-tc oriented along the [110] zone axis, exhibiting a hexagonal projection comprising two {100} and two {111} facets. HRTEM analysis resolved distinct lattice spacings of 0.214 nm and 0.305 nm (Figure 3e), corresponding precisely to the (200) and (111) planes of Cu_2O, respectively. While Cu_2O-o in Figure 3c also exhibited a hexagonal projection, this morphology originated from the [111] zone axis (distinct from the orientation in Figure 3b). This projection revealed a regular hexagon formed by four {111} facets, delineated by red dashed lines. HRTEM confirmed the {111} identity of these facets (Figure 3f). This is consistent with the surface terminations for these three nanostructures of Cu_2O reported in the literature. The corresponding SAED patterns in Figure 3g–i provided compelling evidence supporting these observations.

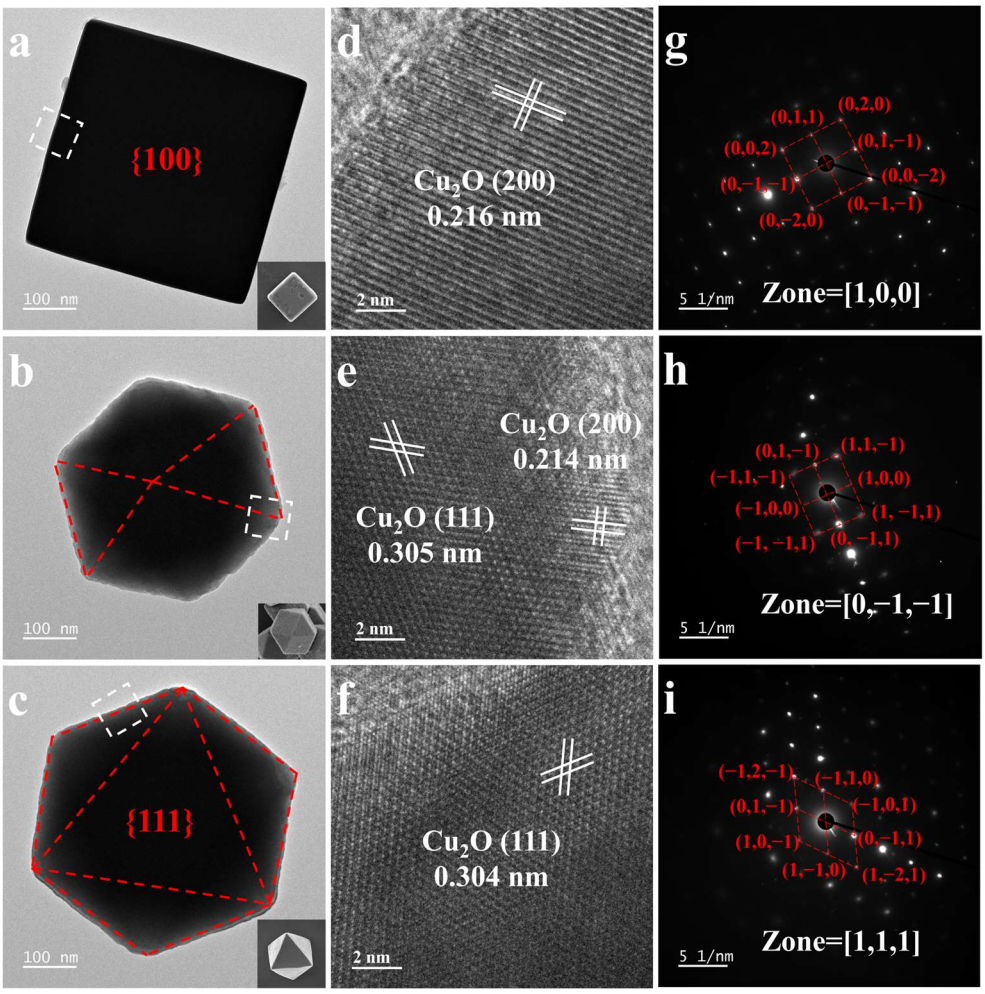

Figure 3. The detailed crystallographic features of the Cu_2O nanocrystals. (**a**,**b**,**c**) The bright TEM images, (**d**,**e**,**f**) high-resolution TEM (HRTEM) images, (**g**,**h**,**i**) the corresponding SAED of Cu_2O-c, Cu_2O-tc, and Cu_2O-o, respectively. The white square border in (**a**–**c**) represents the selected area on the sample to be enlarged for HRTEM, the facets composed by the red dashed lines represent the {111} facets.

To investigate the influence of distinct crystal planes on the reaction of silicon and alcohol, complete removal of PVP from the Cu_2O surface was essential to ensure full exposure of the targeted planes [42]. Fourier transform infrared (FTIR) spectroscopy was employed to confirm the absence of PVP or other adsorbed organic species on the nanocrystal surfaces (Supporting Information, Figure S3). The FTIR spectra exhibited only one discernible band at 600 cm^{-1}, attributed to the Cu–O lattice vibration, and no detectable peaks within the 2850–2960 cm^{-1} range characteristic of C–H stretching vibrations. This absence confirmed the effective removal of PVP. The X-ray photoelectron (XPS) spectrum of Cu_2O provided further evidence that PVP does not exist on the particle surface (Figure 4a). Additionally, the XPS spectrum was used to analyze the elemental composition and copper oxidation state within the Cu_2O crystals, clearly confirming consistent elemental composition (Cu and O) for Cu_2O-c, Cu_2O-tc, and Cu_2O-o. As shown in Figure 4b, the Cu 2p spectra of all the samples were deconvoluted into two sets of spin–orbit split doublets, which were assigned to Cu^+ (low binding energy) and Cu^{2+} (high binding energy). The peaks (areas filled with light color) located at 932.5 and 952.4 eV belong to the Cu^+ $2p_{3/2}$ and Cu^+ $2p_{1/2}$ characteristic peaks. The peaks located at 934.8 and 954.9 eV belong to the characteristic peaks of Cu^{2+} $2p_{3/2}$ and Cu^{2+} $2p_{1/2}$. Since only weak satellite peaks occur at 943.9 and 962.8 eV instead of obvious shaking up peaks, this is a key feature that distinguishes it from Cu^{2+}. It should be noted that the overlapping binding energies of Cu^+ and Cu^0 precluded their differentiation in the Cu 2p spectra [43], thus the Cu LMM Auger electron spectroscopy was used to distinguish Cu^+ from Cu^0 (Figure 4c). There was only one apparent peak at around

916.6 eV which indicates that no Cu^0 exists in the system since it is widely acknowledged that Cu^+ and Cu^0 were situated at 916.8 eV and 918.6 eV.

O 1s XPS spectra were also measured to study the different oxygen species on the surface of the three Cu_2O samples. The spectra were deconvoluted into three contributions assignable to distinct oxygen chemical states (Figure 4d). The peaks, separately with lower binding energy (530.1 eV) and higher binding energy (532.8 eV), were ascribed to lattice oxygen (O^{2-}) labelled as O_{latt} and hydroxyl oxygen (OH^-), respectively. The peak at intermediate binding energy (531.2 eV) was indicative of adsorbed oxygen at vacancy sites (O^- or O_2^{2-}), denoted as O_{ads} [44,45]. To ensure the accuracy of the calculation, the C 1s spectrum provided evidence that the sample was not affected by carbon contamination. The sample might adsorb carbonates when exposed to air, but only one C-C characteristic peak was shown in Figure S4, the C-O/C=O and other oxidation state characteristic peaks were hardly visible. Therefore, the influence of carbon contamination on the quantitative analysis of O 1s could be excluded. Quantitative analysis of O 1s spectra yielded the surface molar percentages of O_{latt} and O_{ads} (Table S2). O_{ads}/O_{latt} molar ratio increased from 0.8893 for Cu_2O-c to 0.9934 for Cu_2O-o, indicating enhanced incorporation of adsorbed oxygen during the growth of {111} facets. This suggests that the {111} surfaces likely developed a higher concentration of oxygen vacancies during the reductive synthesis of Cu_2O, which is also consistent with results reported in the literature [46,47]. While Cu^+ metal sites serve as the primary reactive sites in Cu_2O, oxygen species (lattice oxygen, surface oxygen moieties, and oxygen vacancies) frequently participate in auxiliary roles [48]. This synergistic mechanism is consistent with our previous experimental findings demonstrating that Cu_2O exhibits a stronger promoting effect on the reaction compared to CuCl or other Cu^+ based systems. For instance, oxygen vacancies may play a decisive role in ethanol adsorption and dehydrogenation oxidation [49]. Furthermore, the environmental-friendly properties of oxygen have further enhanced the sustainability features of these processes.

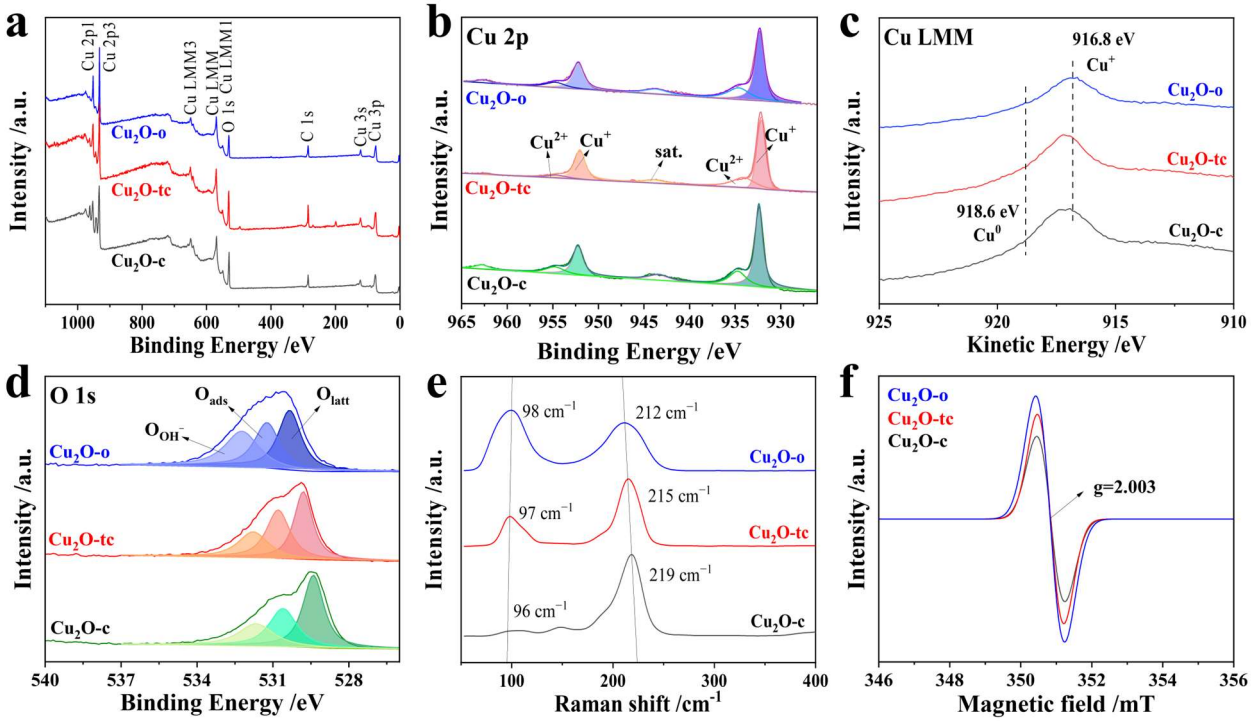

Figure 4. (**a**) XPS spectrum of Cu_2O-c, Cu_2O-tc, and Cu_2O-o, (**b**,**d**) Magnified XPS spectra showing the exact positions of the Cu 2p and O 1s peaks, Cu LMM Auger spectra (**c**), Raman spectroscopy (**e**) and EPR spectroscopy (**f**) of Cu_2O-c, Cu_2O-tc and Cu_2O-o.

3.2. Evaluation of Oxygen Vacancy for Cu_2O with Different Facets

In order to express the existence of oxygen vacancies more clearly, Raman spectroscopy was employed to confirm the presence. The increased oxygen vacancy concentration induced lattice distortion in Cu_2O, altering interatomic bond lengths and angles [30,50]. As shown in Figure 4e, the characteristic Raman peak corresponding to the O–Cu–O bending vibration observed at approximately 220 cm^{-1} exhibited both a red shift (towards lower wavenumbers) along with peak broadening. Furthermore, oxygen vacancies disrupted lattice symmetry, thereby activating Raman-inactive vibrational modes. This symmetry breaking manifested as the emergence of a new peak near 100 cm^{-1}. We further used EPR spectroscopy to probe the concentration of oxygen vacancies in different Cu_2O samples (Figure 4f). The characteristics peak of oxygen vacancies (g = 2.003) [51] in the EPR spectra followed the order of Cu_2O-o > Cu_2O-tc > Cu_2O-c. As a bulk technique, EPR provides the overall information about oxygen vacancies in Cu_2O. The results above showed that Cu_2O-o enclosed by {111} facets exhibited a higher concentration of oxygen vacancies than Cu_2O-tc and Cu_2O-c enclosed by {100} facets, which corresponds to the relatively high oxygen vacancies in the {111} facets surface region as probed by XPS.

Figure S5 shows the optimized (100) and (111) surface structures, the optimized (111) surface exhibits an obvious surface reconstruction. And it can be seen that there are greater amounts of unsaturated Cu dangling bonds and surface oxygen vacancies in the (111) facet, the surface energy of the (100) facet is 7.74 eV/nm^2, and it is larger than that of the (111) facet (4 eV/nm^2). Gao et al. [28] calculated the surface energy of Cu_2O crystals at each crystal facet, among which the (200) face has the highest surface energy, the (111) face has the lowest surface energy, and the preferred growth face is the (200) face. Therefore, the most common crystal structure of Cu_2O is a cube, and the crystal plan is the (200) face. The (100) facet consists of alternating layers of O^{2-} and Cu^{+} and is electrically neutral, giving it relative stability. In contrast, the (111) facet is characterized by an interwoven arrangement of O^{2-} and Cu^{+}, with O^{2-} terminating at the plane edges and exhibiting dangling bonds. The presence of these dangling bonds, along with the unsaturated coordination of Cu^{+}, results in higher reactivity and surface energy for the (111) facet. However, we are unclear how the exposure of different surfaces of Cu_2O microcrystals affects the reaction, so further study is still needed to elucidate the facet-dependent effects of the as-obtained Cu_2O microcrystals.

In addition to oxygen vacancy concentration, the surface hydroxyl oxygen was also found to be related to surface facets. The ratio of O_{latt}/O_{OH^-}, which represents the surface hydroxyl group, increased from Cu_2O-c (100), Cu_2O-tc (100)&(111) to Cu_2O-o (111). The {111} facets exhibited higher hydroxyl group density than the {100} facets, which was also consistent with the results reported in the literature.

The {111} planes exhibit a noticeably higher hydroxyl group concentration than the {100} planes, likely due to the lower adsorption energy of hydroxyl groups on the {111} surfaces. According to Zhong W, et al. [34], the free energy for adsorbing a hydroxyl group on the (111) surface plane was much lower than (100) surface plane. In addition, the higher concentration of oxygen vacancies on the {111} planes can also promote the dissociation of water molecules on the surface to form hydroxyl groups [52,53].

This process was supposed to be equally effective for ethanol molecules as well. Interestingly, DFT results showed that the adsorption energy of ethanol on the perfect (111) surface plane (−0.14 eV, Figure 5b) was actually weaker than that on the perfect (100) surface plane (−0.19 eV, Figure 5a), which seemed to contradict to mentioned above. As demonstrated in the previous section, the (111) surface plane exhibited noticeably higher oxygen vacancies than that of the (100) surface. Therefore, Cu_2O-o (111) with oxygen vacancies ((111)_OV) was constructed to consider the impact of oxygen vacancies on (111) surface on the adsorption of ethanol. The adsorption of ethanol was significantly enhanced on (111) surface with oxygen vacancies (−0.25 eV, Figure 5c), which was noticeably stronger than that on (100) surface plane. These results suggest that the superior adsorption capacity of the Cu_2O-o (111) sample compared to the Cu_2O-c (100) sample arises from the presence of oxygen vacancies on the (111) surface.

Additionally, calculations of density of states (DOS) showed that during ethanol adsorption on the Cu_2O-o (111) surface, the d-band center of the surface copper atoms (−1.89 eV) was closer to the Fermi level compared to Cu_2O-c (100) surface (−3.01 eV, Figure 5d,e). When oxygen vacancies were introduced, the d-band center shifted even closer to the Fermi level (−1.58 eV, Figure 5f). According to d-band theory, the upshift in the d-band center enhances the antibonding orbital interaction between Cu and ethanol, reducing electron occupancy in the anti-bonding orbital, thus strengthening the adsorption and activation of ethanol. These electronic structural features indicate a stronger interaction between the Cu_2O-o (111) facet and ethanol molecules, particularly in the presence of oxygen vacancies. Recent studies have shown that when oxygen vacancies are created on the oxide surface, the electrons around the copper atoms originally bonded to oxygen atoms undergo a redistribution to maintain charge balance [54,55]. This typically gives rise to a new peak near the Fermi level, referred to as a "defect state" or "localized state". Consequently, the d-band center of the adjacent copper atoms shifts toward the Fermi level. This is a key change, implying that the d-orbital electrons of the surface copper atoms are raised in energy, thereby facilitating electron back-donation to the adsorbed ethanol molecules, thereby enhancing surface chemisorption capability and chemical reactivity [56].

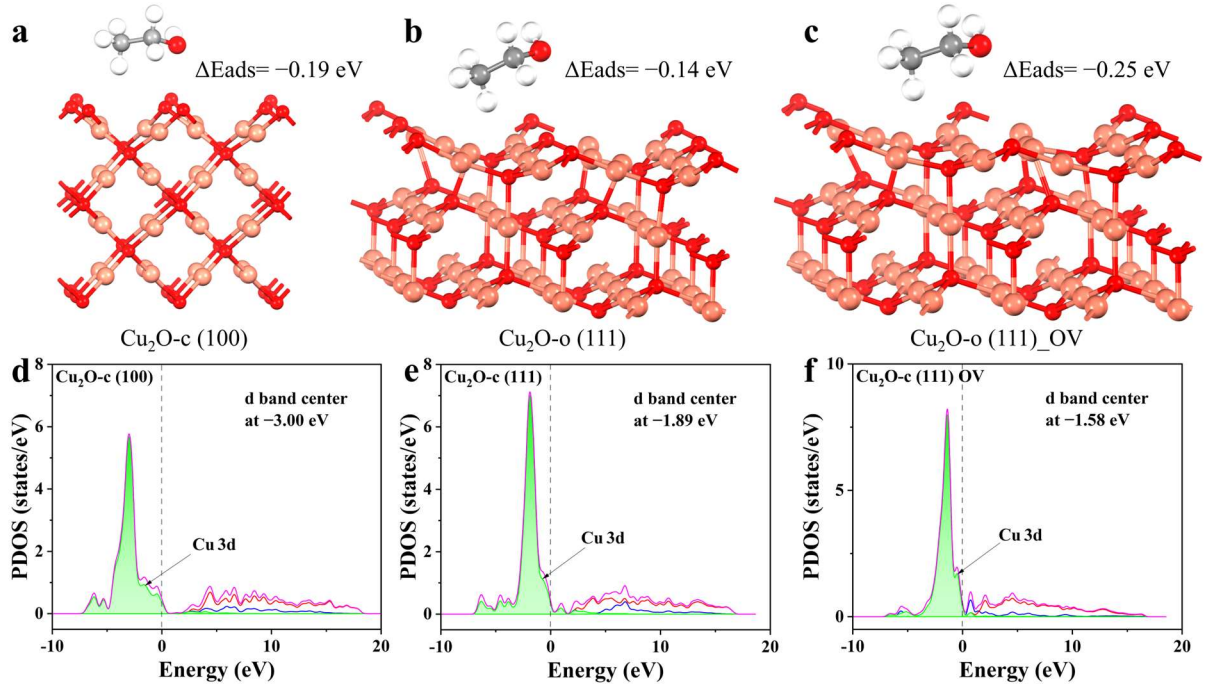

Figure 5. Structural model of exposed crystal facet after adsorption of ethanol: (**a**) side view of the Cu_2O-c (100) surface, (**b**) side view of the Cu_2O-o (111) surface, (**c**) side view of the Cu_2O-o (111)_OV surface. The red and pink balls represent oxygen and copper atoms, respectively. D-band center calculations at specific ethanol adsorption sites on (**d**) Cu_2O-c (100), (**e**) Cu_2O-o (111), and (**f**) Cu_2O-o (111)_OV surfaces.

3.3. Influence of Facet-Dependent Performance in Direct Synthesis of TEOS

In the study of the direct reaction, the particle size and specific surface area effects are inherent properties of Cu_2O under different morphologies, and thus deliberately excluded from the investigation conditions. Under identical reaction conditions, only the type of Cu_2O with different exposed crystal planes was varied. Three representative Cu_2O samples with distinct morphologies (Cu_2O-c, Cu_2O-tc, and Cu_2O-o) were selected from the morphological evolution series. These samples were evaluated under identical mass conditions, and the reaction time, silicon conversion, and TEOS yield were determined for each. Reaction time was monitored via an autoclave-mounted pressure gauge. As shown in Equations (1) and (2), H_2 is generated during the reaction, and the pressure rise resulting from H_2 evolution far exceeds the fluctuations

in saturated vapor pressure caused by changes in the boiling point of the reaction mixture. Consequently, the reactor pressure exhibited a continuous upward trend, with a sharp rise in the gauge readings observed during periods of intense reaction. Thus, pressure variations provided an indirect method for monitoring the internal state of reactor. The reaction endpoint was designated as the time when the pressure rise slowed markedly or ceased entirely, and this time was recorded as the reaction time. As shown in Table 1, Cu_2O-c gave a conversion rate of 90.2% and a yield of 82.7% after 7 h of reaction, whereas Cu_2O-tc delivered a 94.7% conversion rate and a 84.8% yield in 3 h. Although the conversion and yield values remained comparable, the significant reduction in reaction time indicates that Cu_2O-tc has a higher promoting efficiency than Cu_2O-c in this reaction. Remarkably, Cu_2O-o achieved a 92.5% yield after just 1 h of reaction. Cu_2O-o was clearly the best and most efficient samples among these nanocrystal morphologies (*i.e.*, Cu_2O-o > Cu_2O-tc > Cu_2O-c), the differences in chemical reactivity were mainly attributed to different exposed crystal planes (*i.e.*, {111} > {111}&{100} > {100}). By comparison, the commercially available Cu_2O powder showed 69.6% yield in 9 h. When Cu_2O was not present, after a 9-h reaction, only a very small amount of conversion rate and yield were achieved. This performance disparity primarily stems from the well-defined morphology and controlled particle size of the laboratory-synthesized Cu_2O crystals. And in other reaction temperature and time conditions, the reactivity of Cu_2O-o failed to achieve optimal efficiency. A decrease in reaction temperature led to a marked decline in efficiency, while the reaction time exerted a relatively small influence on conversion rate and yield (Table S3).

Table 1. Comparison of the reactivity of different Cu_2O nanocrystals for the direct synthesis of TEOS from Si_{met} and EtOH.

Entry	Additive	Reaction Time (h)	Conversion Rate [a]	Yield [b]
1	Cu_2O-c	7	90.2%	82.7%
2	Cu_2O-tc	3	94.7%	84.8%
3	Cu_2O-o	1	99.9%	92.5%
4	Cu_2O (commercial)	9	81.5%	69.6%
5	blank	9	1.5%	0.4%

[a] Conversion rate based on Si_{met}. [b] Yield of major product: TEOS

GC-MS analysis was used to confirm the composition of the product. The product components separated by boiling point entered the mass spectrometer via a heated transfer line and were ionized. Ions were then separated by mass-to-charge ratio (m/z) in the analyzer, generating mass spectra (reflecting fragment patterns) and a total ion chromatogram (TIC, Figure 6). The TIC displayed several distinct peaks, the peak at RT 1.624 min matched ethanol (reaction solvent) in the NIST mass spectral library, the predominant peak at RT 4.648 min was identified as TEOS. Additionally, two minor peaks at RT 3.329 min and RT 7.325 min corresponded to TES and hexaethoxydisiloxane (HEODS), respectively. The presence of TES could be attributed to differences in selectivity, but the presence of HEODS indicated that TEOS had undergone hydrolysis condensation [9–12,57]. Although there was no moisture in the closed reactor system, and we replaced the air in the reactor with dry N_2 before the reaction to ensure a water-free environment, it could have been produced via reactant pathways. For example, in Equations (3)–(5), H_2O may come from the reduction of Cu_2O or other unexpected ways [25]. In order to verify the universality of the "direct synthesis", we conducted studies on other branched alcohols. A similar situation occurred when the solvent was replaced by methanol, resulting in the product tetramethoxysilane (TMOS), with the presence of a dimer (Figure S6).

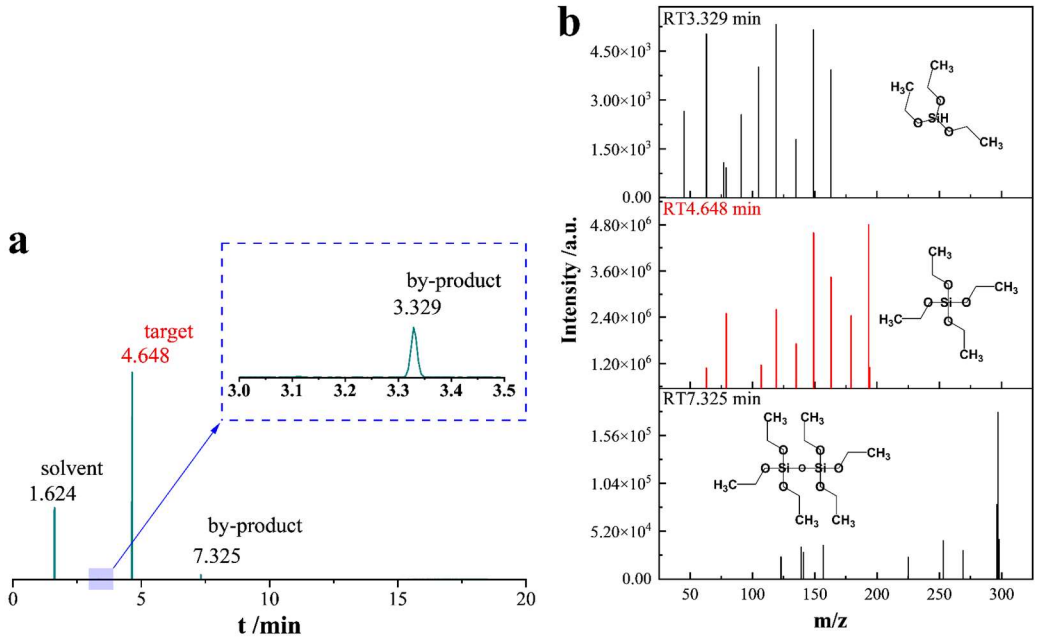

Figure 6. (**a**) Total ion chromatogram and (**b**) mass spectra of TEOS under different retention time.

X-ray fluorescence (XRF) analysis confirmed the high purity (99.43%, Table S1, Supporting Information) of the silicon powder used as the raw material in this study. Nevertheless, ambient oxidation forms a dense native oxide layer (2–3 Å thickness) on the powder surface. This ultrathin amorphous passivation layer escapes detection by XRD due to its sub-nanometer thickness and non-crystalline structure. Critically, this oxide layer will inhibit the reaction between silicon powder and EtOH. XPS was performed to characterize the surface composition and chemical states. It will be readily apparent from Figure 7a that the Si 2p spectrum exhibited two distinct peaks, the peak at lower binding energy corresponded to elemental silicon (Si^0), while the peak at higher binding energy was characteristic of silicon oxide (SiO_2). Notably, a detectable oxide layer was present even on freshly ground silicon powder. After one week of ambient exposure, the SiO_2 peak intensity increased significantly relative to the Si^0 peak. Consistent with this surface passivation, untreated silicon powder exhibited negligible reactivity with ethanol and very low conversion. Based on our previous experience of corroding quartz sand through fluorination reactions [13], an appropriate concentration of NH_4F was reactive with silicon oxide, which provides us with a pretreatment method for silicon powder. After appropriate treatment, the Si^0 peak maintained high intensity and stability over extended periods (Figure 7b), indicating a persistent oxide-free surface and enabling sustained high reactivity.

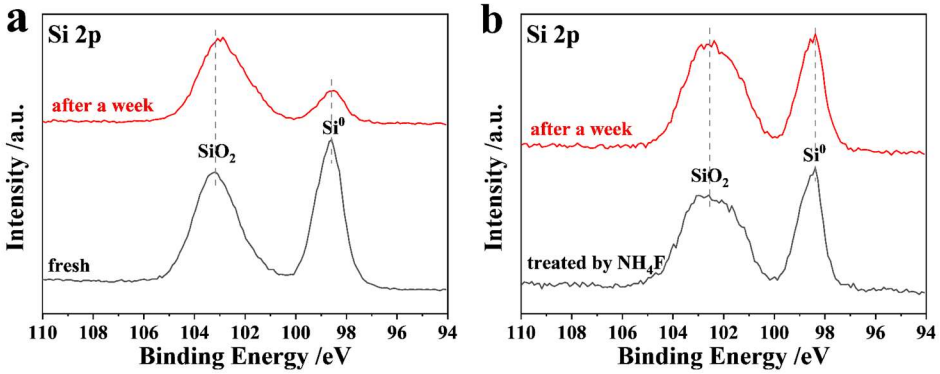

Figure 7. The variation of Si 2p XPS spectra over time during the storage of untreated silicon powder (**a**) and treated by NH_4F (**b**).

It should be noted that the recovery of Cu_2O samples remains a critical consideration for practical implementation. Effective recovery and reuse significantly reduce production costs and enhance industrial viability [58]. Phase composition analysis of solid materials was performed before and after the reaction. As shown in Figure 8a, the solid-phase material prior to the reaction consisted mainly of elemental silicon. The intensity of the Cu_2O peak was relatively weak, but the crystal phase of Cu_2O could still be clearly observed. The activated phase was protected by N_2 and showed no obvious changes. The residue after the reaction no longer shows a clear silicon phase because the silicon powder was consumed during the reaction. As the silicon powder was completely consumed, the dispersed copper species were re-collected. However, during the detection, it was found that the copper species after the reaction had transformed into a new crystal phase of metallic Cu (PDF#04-0836), indicating reduction of the Cu_2O material to Cu. Based on the composition within the reactor system, it can be inferred that H_2 is the only reducing component and has reduced Cu_2O. Additionally, the presence of Cu^{2+} was detected in the Cu 2p spectrum (Figure 8b), which might be attributed to the disproportionation reaction of the Cu_2O. Crystal facet effects significantly influence the disproportionation tendency, with the {111} facets exhibiting the highest propensity due to its elevated surface energy and oxygen vacancy concentration. Tissot et al. [59] provided a more detailed mechanism explanation, when hydrogen interacts with the surface of Cu_2O, hydrogen atoms adsorb on the oxygen sites to form hydroxyl groups, and then H_2 is formed through the disproportionation reaction. Scanning tunneling microscopy and XPS analyses reveal the formation of metallic copper clusters on the Cu_2O surfaces after cycles of hydrogen exposure and annealing. The valence state of the Cu species was further proved by the Cu LMM spectrum (Figure 8c). Since the reactor vessel was sealed, the disproportionation reaction of Cu_2O was inevitable at this stage, which prevented the effective recovery of the Cu_2O sample. However, we propose that the durability of Cu_2O as a catalyst can be effectively evaluated in a fluidized-bed reactor, the detailed catalytic cycle and the exact nature of the active species would be elucidated in future work.

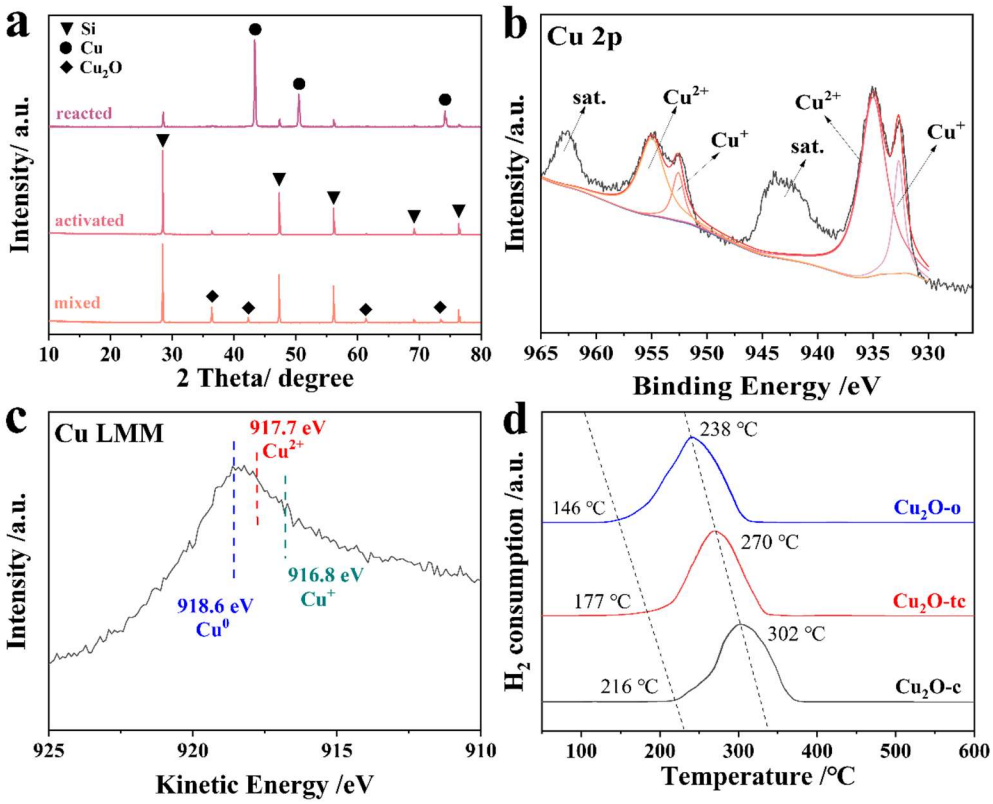

Figure 8. (**a**) XRD patterns of solid-phase material at different stages of the reaction, Cu 2p XPS spectra (**b**) and Cu LMM Auger spectra (**c**) of copper species after the reaction, (**d**) The H_2-TPR curves of Cu_2O-c, Cu_2O-tc, and Cu_2O-o.

The reducibility of Cu_2O was quantitatively assessed by H_2-TPR in 10% H_2/Ar (Figure 8d). The three distinct forms of Cu_2O investigated exhibited a reduction peak, corresponding to the complete reduction of Cu^+ to Cu^0 [60]. The reduction onset temperature progressively decreased across the morphological series from cubic to octahedral Cu_2O (Cu_2O-c (216 °C) > Cu_2O-tc (177 °C) > Cu_2O-o (146 °C)). Quantitative analysis revealed hydrogen consumption values of 2921.43, 2708.12, and 2581.22 μmol/g for Cu_2O-o, Cu_2O-tc, and Cu_2O-c, respectively, confirming the superior reducibility of Cu_2O-o. Stoichiometric analysis of the closed reactor system indicated that complete reaction generates 0.7 mol H_2, substantially exceeding the 0.44 mol required for full reduction of 0.5 g Cu_2O. This confirms in-situ reduction of Cu_2O to Cu by reaction-derived H_2. Furthermore, the H_2-TPR results demonstrate that Cu_2O-o possesses the highest redox activity. The promotional effect of Cu_2O was attributed to the redox behavior of copper species. The balance between the oxidation and reduction rates was important for the overall reaction performance [31].

Certain reports propose that metallic copper promotes the conversion of TES to TEOS [4,19,61]. Specifically, it has been suggested that Cu_2O promotes the silicon-alcohol reaction to form TES (Equation (1)), while the byproduct H_2 reduces Cu_2O to Cu. The resulting metallic copper is then proposed to facilitate the ethoxylation of TES (Equation (2)), implying that the conversion in Equation (2) relies on the presence of copper. To address this mechanistic uncertainty, verification experiments were performed. Analytically pure TES and EtOH were reacted stoichiometrically in identical reactors. We examined the promoting effects using Cu, Cu_2O, and a blank control without Cu_2O. GC-MS analysis revealed identical product profiles across all groups (Figure S7). TIC displayed two peaks at retention times 8.786 min and 11.753 min, identified as TEOS and HEODS, respectively, via mass spectral library matching. Absence of impurities confirmed successful TEOS synthesis under all conditions with high selectivity, including blank group. Pressure monitoring revealed critical kinetic differences (Figure S8). The three groups of experiments exhibited nearly identical pressure curves. During 0~100 min (heating phase), the pressure changes in the system came from the vapor pressure of the solvent. Upon reaching the reaction temperature (200 °C), the generation of H_2 led to a rapid increase in pressure to about 6 MPa. The system with Cu_2O achieved the same final pressure. However, the sudden change in pressure occurred earlier, and the endpoint was reached significantly faster with Cu_2O, indicating its promoting effect on the ethoxylation of TES to TEOS.

4. Conclusions

In summary, this work systematically investigated the crystal facet-dependent reactivity of Cu_2O in the direct synthesis of tetraethoxysilane (TEOS) from metallic silicon and ethanol—a green alternative to the conventional chlorosilane route. By systematically tuning PVP concentration, Cu_2O morphology evolved from {100} facet-enclosed cubes (Cu_2O-c) through truncated cubes (Cu_2O-tc) to {111} facet-exposed octahedrons (Cu_2O-o), as confirmed by electron microscopy and XRD analyses. Comprehensive characterizations, including XPS, Raman, and EPR spectroscopy, revealed that {111} facets possess significantly higher oxygen vacancy concentrations and surface hydroxyl densities compared to {100} facets. Density functional theory (DFT) calculations demonstrated that oxygen vacancies on {111} surfaces substantially enhance ethanol adsorption energy (from −0.14 eV to −0.25 eV), overcoming the intrinsically weaker adsorption on perfect {111} planes. In evaluating the reaction performance under identical conditions, Cu_2O-o exhibited superior performance, achieving 99.9% silicon conversion and 92.5% TEOS yield within 1 h, better than Cu_2O-c (90.2% conversion, 82.7% yield, 7 h) and commercial Cu_2O (81.5% conversion, 69.6% yield, 9 h). The reactivity followed the order of {111} > {111}&{100} > {100} facets. Mechanistic investigations revealed that in-situ generated H_2 reduces Cu_2O to metallic Cu during reaction, with H_2-TPR confirming the superior reducibility of {111}-enriched Cu_2O (reduction onset at 146 °C). This also limited the reusability of the Cu_2O material. However, we also confirmed that the species responsible for promoting the formation of TEOS from TES was not the reduced metallic copper, challenging previous literature assumptions. Furthermore, NH_4F pretreatment effectively removed the native oxide layer from

silicon powder, thereby maintaining surface reactivity, as evidenced by XPS. This work established clear facet-dependent principles for Cu_2O in direct TEOS synthesis, identified oxygen vacancies as key descriptors for reactivity enhancement, and provided structure–reactivity correlations that may guide the design of efficient reaction systems for green organosilicon manufacturing.

Supplementary Materials

The following supporting information can be found at: https://www.sciepublish.com/article/pii/1249, Figure S1. Top view and side view for different models: (a) Cu_2O (100), (b) Cu_2O (111), and (c) Cu_2O (111)_OV slab. The red and pink balls represent oxygen and copper atoms, respectively; Figure S2. XRD patterns of Cu_2O crystals with different geometries, (a) cubes, (b) truncated cubes, (c,d) vertex-truncated octahedrons, (e) octahedrons. The left part is the standard XRD data of bulk Cu_2O. The left part shows the enlarged image of (200) peaks, it can be concluded that the intensity ratio of (111)/(200) increased as the shape of the products evolved from cubes through truncated cubes, vertex-truncated octahedrons and finally to octahedrons; Figure S3. FTIR spectroscopy of Cu_2O crystals with different geometries, (a) cubes, (b) truncated cubes, (c,d) vertex-truncated octahedrons, (e) octahedrons; Figure S4. XPS spectra with C 1s of Cu_2O with different morphologies; Figure S5. Optimized structures of Cu_2O (100) and (111) surfaces: (a) side view of the Cu_2O (100) surface, (b) side view of the Cu_2O (111) surface; Figure S6. Total ion chromatogram and mass spectra of TMOS under different retention time; Figure S7. (a) Total ion chromatogram of products under different additive conditions, (b) mass spectra under different retention time; Figure S8. The variation of pressure in the high-pressure reactor over time under different additive conditions; Table S1. The XRF of silicon powder; Table S2. O 1s results of Cu_2O with different morphologies; Table S3. Effect of reaction time and temperature on silicon conversion and TEOS yield.

Acknowledgments

This work was funded by the Natural Science Foundation of Hubei Province, China (No. 2025AFD247, No. 2025AFD315), the Natural Science Foundation of Yichang Municipality, China (No. A25-3-020). The authors appreciate the facility and technical support provided by Hubei Three Gorges Laboratory Analysis and Testing Center. We are also indebted to Hubei Xingfa Chemicals Group Co., Ltd. (China) for generously donating research material for our research.

Author Contributions

J.F.: Writing—original draft, Investigation, Formal analysis, Data curation. Y.R.: Investigation. Z.L.: Project administration, Formal analysis. G.W., S.Q.: Writing—review & editing, Supervision. R.L.: Writing—review & editing, Supervision, Resources, Methodology, Conceptualization. R.C.: Writing—review & editing, Resources, Conceptualization.

Ethics Statement

Not applicable.

Informed Consent Statement

Not applicable.

Data Availability Statement

Data will be made available on request.

Funding

This work was funded by the Natural Science Foundation of Hubei Province, China (No. 2025AFD247, No. 2025AFD315), the Natural Science Foundation of Yichang Municipality, China (No. A25-3-020).

Declaration of Competing Interest

The authors declare that they have no known competing financial interests or personal relationships that could have appeared to influence the work reported in this paper.

References

1. Lin YF, Kuo JW. Mesoporous bis(trimethoxysilyl)hexane (BTMSH)/tetraethyl orthosilicate (TEOS)-based hybrid silica aerogel membranes for CO_2 capture. *Chem. Eng. J.* **2016**, *300*, 29–35. DOI:10.1016/j.cej.2016.04.119
2. Longhi M, Kunsta SR, Beltrami LVR, Kerstner EK, Filho CIS, Sarmento VHV, et al. Effect of tetraethoxy-silane (TEOS) amounts on the corrosion prevention properties of siloxane-PMMA hybrid coatings on galvanized steel substrates. *Mater. Res.* **2015**, *18*, 1140–1155. DOI:10.1590/1516-1439.321614
3. Smith SA, Williams BP, Joo YL. Effect of polymer and ceramic morphology on the material and electrochemical properties of electrospun PAN/polymer derived ceramic composite nanofiber membranes for lithium ion battery separators. *J. Membr. Sci.* **2017**, *526*, 315–322. DOI:10.1016/j.memsci.2016.12.052
4. Temnikov MN, Zhiltsov AS, Kotov VM, Krylova IV, Egorov MP, Muzafarov AM. Comparison of effectiveness of various approaches to direct synthesis of alkoxysilanes. *Silicon* **2015**, *7*, 69–78. DOI:10.1007/s12633-014-9236-9
5. Adonin NY, Prikhod'ko SA, Shabalin AY, Prosvirin IP, Zaikovskii VI, Kochubey DI, et al. The "direct" synthesis of trialkoxysilanes: New data for understanding the processes of the copper-containing active sites formation during the activation of the initial silicon based contact mass. *J. Catal.* **2016**, *338*, 143–153. DOI:10.1016/j.jcat.2016.03.012
6. Laine RM, Furgal JC, Doan P, Pan D, Popova V, Zhang X. Avoiding carbothermal reduction: distillation of alkoxysilanes from biogenic, green, and sustainable sources, *Angew. Chem. Int. Ed.* **2016**, *55*, 1065–1069. DOI:10.1002/anie.201506838
7. Chibiryaev AM, Kozhevnikov IV, Martyanov ON. High-temperature reaction of SiO_2 with methanol: Nucleophilic assistance of some N-unsubstituted benzazoles. *Appl. Catal. A Gen.* **2013**, *456*, 159–167. DOI:10.1016/j.apcata.2013.03.001
8. Fukaya N, Choi SJ, Horikoshi T, Kumai H, Hasegaw M, Yasuda H, et al. Synthesis of tetramethoxysilane from silica and methanol using carbon dioxide and an organic dehydrating reagent. *Chem. Lett.* **2016**, *45*, 828–830. DOI:10.1246/cl.160329
9. Nguyen TTH, Fukaya N, Sato K, Choi J-C, Kataoka S. Technoeconomic and environmental assessment for design and optimization of tetraethyl orthosilicate synthesis process. *Ind. Eng. Chem. Res.* **2018**, *57*, 2192–2199. DOI:10.1021/acs.iecr.7b03895
10. Putro WS, Lee VY, Sato K, Choi J-C, Fukaya N. From SiO_2 to alkoxysilanes for the synthesis of useful chemicals. *ACS Omega* **2021**, *6*, 35186–35195. DOI:10.1021/acsomega.1c05138
11. Fukaya N, Choi SJ, Horikoshi T, Kataoka S, Endo A, Kumai H, et al. Direct synthesis of tetraalkoxysilanes from silica and alcohols. *New J. Chem.* **2017**, *41*, 2224–2226. DOI:10.1039/c6nj03897b
12. Nguyen TTH, Fukaya N, Choi SJ, Sato K, Choi J-C. Impact of the water removal method on tetraethyl orthosilicate direct synthesis: Experiment and process assessment. *Ind. Eng. Chem. Res.* **2019**, *58*, 19997–20002. DOI:10.1021/acs.iecr.9b02887
13. Feng J, Li Z, Liu X, Chi R. Preparation of silica gel from quartz for direct synthesis of alkoxysilanes. *Silicon* **2025**, *17*, 1767–1775. DOI:10.1007/s12633-025-03309-4
14. Seyferth D. Dimethyldichlorosilane and the direct synthesis of methylchlorosilanes. The key to the silicones industry. *Organometallics* **2001**, *20*, 4978–4992. DOI:10.1021/om0109051
15. Hurd DT, Rochow EG. On the mechanism of the reaction between methyl chloride and silicon-copper. *J. Am. Chem. Soc.* **1945**, *67*, 469–471. DOI:10.1021/ja01223a007
16. Newton WE, Rochow EG. Direct synthesis of organic derivatives of silicon using nonhalogenated organic compounds. *Inorg. Chem.* **1970**, *9*, 1071–1075. DOI:10.1021/ic50087a014
17. Han J, Gheyas SI, Wang Y, Strongin DR, Graham AP, Hinch BJ, et al. Thermal chemistry of CH_3 on Si/Cu(100). *J. Phys. Chem. B* **2000**, *104*, 3078–3084. DOI:10.1021/jp9928863
18. Acker J, Bohmhammel K. Thermodynamic assessment of the copper catalyzed direct synthesis of methylchlorosilanes. *J. Organomet. Chem.* **2008**, *693*, 2483–2493. DOI:10.1016/j.jorganchem.2008.04.026

19. Adonin NY, Prikhod'ko SA, Shabalin AY, Prosvirin IP, Zaikovskii VI, Kochubey DI, et al. Synthesis and structural features of nanostructured cuprous chloride with high catalytic activity. *Silicon* **2015**, *7*, 79–87. DOI:10.1007/s12633-014-9272-5
20. Zhang Z, Che H, Wang Y, She X, Sun J, Gunawan P, et al. Facile solvothermal synthesis of porous cubic Cu microparticles as copper catalysts for Rochow reaction. *ACS Appl. Mater. Interfaces* **2012**, *4*, 1295–1302. DOI:10.1021/am3002605
21. Zhang Z, Che H, Wang Y, Gao J, She X, Sun J, et al. Flower-like CuO microspheres with enhanced catalytic performance for dimethyldichlorosilane synthesis. *RSC Adv.* **2012**, *2*, 2254–2256. DOI:10.1039/C2RA00923D
22. Zhang Z, Che H, Gao J, Wang Y, She X, Sun J, et al. Shape-controlled synthesis of Cu_2O microparticles and their catalytic performances in the Rochow reaction. *Catal. Sci. Technol.* **2012**, *2*, 1207–1212. DOI:10.1039/C2CY20070H
23. Zhang Z, Che H, Wang Y, Gao J, Zhao L, She X, et al. Facile synthesis of mesoporous Cu_2O microspheres with improved catalytic property for dimethyldichlorosilane synthesis. *Ind. Eng. Chem. Res.* **2012**, *51*, 1264–1274. DOI:10.1021/ie2020747
24. Li J, Ni Z, Ji Y, Zhu Y, Liu H, Zhang Y, et al. ZnO supported on Cu_2O{100} enhances charge transfer in dimethyldichlorosilane synthesis. *J. Catal.* **2019**, *374*, 284–296. DOI:10.1016/j.jcat.2019.02.029
25. Krylova IV, Egorov MP, Nefedov OM. Reaction of silicon with alcohols in autoclave. *Russ. Chem. Bull.* **2017**, *66*, 260–266. DOI:10.1007/s11172-017-1726-7
26. Su K, Ji Y, Zhou X, Jiang X, Li H, Zhu Y, et al. Approach to generating the right active phase in the "Direct" synthesis of trimethoxysilanes using the CuCl-Cu_2O catalyst. *Appl. Surf. Sci.* **2021**, *544*, 148915. DOI:10.1016/j.apsusc.2020.148915
27. Su G, Wang A, Zhang M, Yin H, Wang G. Selective Synthesis of Triethoxysilane and Tetraethoxysilane through Direct Reaction between Ethanol and Silicon Catalyzed by CuCl and Metallic Cu0 Nanoparticles in Fixed-bed Reactor. *Silicon* **2020**, *14*, 573–580. DOI:10.1007/s12633-020-00830-6
28. Gao Y, Zhang L, van Hoof AJF, Hensen EJM. On the surface-dependent oxidation of Cu_2O during CO oxidation: Cu^{2+} is more active than Cu^{+}. *Appl. Catal. A Gen.* **2020**, *602*, 117712. DOI:10.1016/j.apcata.2020.117712
29. Huang W, Liu Q, Zhou Z, Li Y, Ling Y, Wang Y, et al. Tuning the activities of cuprous oxide nanostructures via the oxide-metalinteraction. *Nat. Commun.* **2020**, *11*, 2312. DOI:10.1038/s41467-020-15965-8
30. Li J, He M, Yan J, Liu J, Zhang J, Ma J. Room temperature engineering crystal facet of Cu_2O for photocatalytic degradation of methyl orange. *Nanomaterials* **2022**, *12*, 1697. DOI:10.3390/nano12101697
31. Sun X-L, Yuan H, Yang D, Hu Z. Synergism between {111} and {100} crystal facets on Cu_2O for boosted photothermal catalysis. *Ind. Eng. Chem. Res.* **2025**, *64*, 1046–1057. DOI:10.1021/acs.iecr.4c03649
32. Teng Z, Yi X, Zhang C, He C, Yang Y, Hao Q, et al. CO self-sustained catalytic combustion over morphological inverse model CeO_2/Cu_2O catalysts exposing (100), (111) and (110) planes. *Appl. Catal. B Environ.* **2023**, *339*, 123119. DOI:10.1016/j.apcatb.2023.123119
33. Wan L, Zhou Q, Wang X, Wood TE, Wang L, Duchesne PN, et al. Cu_2O nanocubes with mixed oxidation-state facets for (photo)catalytic hydrogenation of carbon dioxide. *Nat. Catal.* **2019**, *2*, 889–898. DOI:10.1038/s41929-019-0338-z
34. Zhong W, Gong Z, He Z, Zhang N, Kang X, Mao X, et al. Modulating surface oxygen species via facet engineering for efficient conversion of nitrate to ammonia. *J. Energy Chem.* **2023**, *78*, 211–221. DOI:10.1016/j.jechem.2022.11.024
35. Xiong W, Gu X-K, Zhang Z, Chai P, Zang Y, Yu Z, et al. Author correction: fine cubic Cu_2O nanocrystals as highly selective catalyst for propylene epoxidation with molecular oxygen. *Nat. Commun.* **2021**, *12*, 5921. DOI:10.1038/s41467-021-26257-0
36. Zhao X, Susman MD, Rimer JD, Bollini P. Synthesis, structure, and catalytic properties of faceted oxide crystals. *ChemCatChem* **2020**, *13*, 6–27. DOI:10.1002/cctc.202001066
37. Perdew JP, Burke K, Ernzerhof M. Generalized gradient approximation made simple. *Phys. Rev. Lett.* **1996**, *77*, 3865–3868. DOI:10.1103/PhysRevLett.77.3865
38. Li L, Zhang R, Vinson J, Shirley EL, Greeley JP, Guest JR, et al. Imaging catalytic activation of CO_2 on Cu_2O (110): A first-principles study. *Chem. Mater.* **2018**, *30*, 1912–1923. DOI:10.1021/acs.chemmater.7b04803
39. Huang W-C, Lyu L-M, Yang Y-C, Huang M-H. Synthesis of Cu_2O nanocrystals from cubic to rhombic dodecahedral structures and their comparative photocatalytic activity. *J. Am. Chem. Soc.* **2012**, *134*, 1261–1267. DOI:10.1021/ja209662v
40. Chen B-H, Kumar G, Wei Y-J, Ma H-H, Kao J-C, Chou P-J, et al. Experimental revelation of surface and bulk lattices in faceted Cu_2O crystals. *Small* **2023**, *19*, 230491. DOI:10.1002/smll.202303491
41. Zhang D-F, Zhang H, Guo L, Zheng K, Han X-D, Zhang Z. Delicate control of crystallographic facet-oriented Cu_2O nanocrystals and the correlated adsorption ability. *J. Mater. Chem.* **2009**, *19*, 5220–5225. DOI:10.1039/B816349A
42. Yin Y, Liu K, Gao M, Zhang L, Su H, Zeng S. Influence of the structure and morphology of CuO supports on the amount and properties of copper–cerium interfacial sites in inverse CeO_2/CuO catalysts. *J. Mol. Catal. A Chem.* **2015**, *404–405*, 193–203. DOI:10.1016/j.molcata.2015.05.001

43. Biesinger MC, Lau LWM, Gerson AR, Smart RSC. Resolving surface chemical states in XPS analysis of first row transition metals, oxides and hydroxides: Sc, Ti, V, Cu and Zn. *Appl. Surf. Sci.* **2010**, *257*, 887–898. DOI:10.1016/j.apsusc.2010.07.086
44. Yuan Q, Chen L, Xiong M, He J, Luo S-L, Au C-T, et al. $Cu_2O/BiVO_4$ heterostructures: Synthesis and application in simultaneous photocatalytic oxidation of organic dyes and reduction of Cr(VI) under visible light. *Chem. Eng. J.* **2014**, *255*, 394–402. DOI:10.1016/j.cej.2014.06.031
45. Li S, Wang H, Li W, Wu X, Tang W. Effect of Cu substitution on promoted benzene oxidation over porous CuCo-based catalysts derived from layered double hydroxide with resistance of water vapor. *Appl. Catal. B Environ.* **2015**, *166–167*, 260–269. DOI:10.1016/j.apcatb.2014.11.040
46. Zhu Y, Zhang L, Zhao B, Chen H, Liu X, Zhao R, et al. Improving the activity for oxygen evolution reaction by tailoring oxygen defects in double perovskite oxides. *Adv. Funct. Mater.* **2019**, *29*, 1901783.1–1901783.12. DOI:10.1002/adfm.201901783
47. Liu B, Yao X, Zhang Z, Li C, Zhang J, Wang P, et al. Synthesis of Cu_2O nanostructures with tunable crystal facets for electrochemical CO_2 reduction to alcohols. *ACS Appl. Mater. Interfaces* **2021**, *13*, 39165–39177. DOI:10.1021/acsami.1c03850
48. Nandy S, Thapa R, Kumar M, Som T, Bundaleski N, Teodoro OMND, et al. Efficient field emission from vertically aligned $Cu_2O_{1-\delta}(111)$ nanostructure influenced by oxygen vacancy. *Adv. Funct. Mater.* **2015**, *25*, 947–956. DOI:10.1002/adfm.201402910
49. Wang J, Chen L, Yue L, Filot IAW, Hensen EJM, Liu P. Unveiling the Au-Mn-Cu synergy in $Au/LaMnCuO_3$ catalysts for selective ethanol oxidation. *Chin. J. Catal.* **2025**, *75*, 34–48. DOI:10.1016/S1872-2067(25)64686-9
50. Zhang R, Teoh WY, Amal R, Chen B, Kaliaguine S. Catalytic reduction of NO by CO over $Cu/Ce_xZr_{1-x}O_2$ prepared by flame synthesis. *J. Catal.* **2010**, *272*, 210–219. DOI:10.1016/j.jcat.2010.04.001
51. Zhu Y, Zhong X, Jin S, Chen H, He Z, Liu Q, et al. Oxygen defect engineering in double perovskite oxides for effective water oxidation. *J. Mater. Chem. A* **2020**, *8*, 10957–10965. DOI:10.1039/D0TA04362A
52. Zhu Y, He Z, Choi Y, Chen H, Li X, Zhao B, et al. Tuning proton-coupled electron transfer by crystal orientation for efficient water oxidization on double perovskite oxides, *Nat. Commun.* **2020**, *11*, 4299. DOI:10.1038/s41467-020-17657-9
53. Wu C, Sun Y, Wen X, Zhang J-Y, Qiao L, Cheng J, et al. Adjusting oxygen vacancies in perovskite $LaCoO_3$ by electrochemical activation to enhance the hydrogen evolution reaction activity in alkaline condition, *J. Energy Chem.* **2023**, *76*, 226–232. DOI:10.1016/j.jechem.2022.08.035
54. Fernández HM, Amirabbasi M, Mempin C, Jr., Trapletti A, Wartner G, Tesch MF, et al. Plasma-engineered hydroxyl defects in NiO: A DFT-Supported-Spectroscopic analysis of oxygen-hole states and implications for water oxidation. *J. Am. Chem. Soc.* **2026**, *148*, 15076–15091. DOI:10.1021/jacs.6c00210
55. Pan Y, Li R, Zhang L, Liu J-X, Wang W, Zhang G-J. Synergistic mechanochemistry and facet engineering boost conversion of dilute CO_2 from industrial flue gases. *Appl. Catal. B Environ.* **2026**, *391*, 126686. DOI:10.1016/j.apcatb.2026.126686
56. Liao S, Xu S, Ye L, Gu Y-C, Li J, Hu C. Facet-engineered Cu_2O microcrystals for tailoring biomass-polyol conversion to glycolic acid. *Appl. Catal. B Environ.* **2026**, *393*, 126762. DOI:10.1016/j.apcatb.2026.126762
57. Lee HR, Shibata T, Kanezashi M, Mizumo T, Ohshita J. Pore-size-controlled silica membranes with disiloxane alkoxides for gas separation. *J. Membr. Sci.* **2011**, *383*, 152–158. DOI:10.1016/j.memsci.2011.08.046
58. Vuyyuru KR, Pant KK, Krishnan VV, Nigam KDP. Recovery of nickel from spent industrial catalysts using chelating agents. *Ind. Eng. Chem. Res.* **2010**, *49*, 2014–2024. DOI:10.1021/ie901406e
59. Tissot H, Wang C, Stenlid JH, Panahi M, Kaya S, Soldemo M, et al. Interaction of atomic hydrogen with the $Cu_2O(100)$ and (111) surfaces. *J. Phys. Chem. C* **2019**, *123*, 22172–22180. DOI:10.1021/acs.jpcc.9b03888
60. Kim JY, Rodriguez JA, Hanson JC, Frenkel AI, Lee PL. Reduction of CuO and Cu_2O with H_2: H embedding and kinetic effects in the formation of suboxides. *J. Am. Chem. Soc.* **2003**, *125*, 10684–10692. DOI:10.1021/ja0301673
61. Nguyen TTH, Kataoka S, Fukaya N, Sato K, Choi J-C, Endo A. Feasibility study of new synthesis route of tetraethoxysilane from rice hull ash. *Comput. Aided Chem. Eng.* **2017**, *40*, 703–708. DOI:10.1016/B978-0-444-63965-3.50119-7